Applied Ocean Research 164 (2025) 104787

Contents lists available at ScienceDirect

Applied Ocean Research

journal homepage: www.elsevier.com/locate/apor

Research paper

A comparative experimental study of the hydrodynamic force on a solid heave plate, and on heave plates with regularly distributed and fractally distributed perforations

Antonio Medina-Manuel [a], Trygve Kristiansen [b,*], Adolfo Maron-Loureiro [c], Rafael Molina Sánchez [d], Antonio Souto-Iglesias [a]

[a] CEHINAV, DACSON, ETSIN, Universidad Politécnica de Madrid (UPM), 28040 Madrid, Spain
[b] Department of Marine Technology, Norwegian University of Science and Technology (NTNU), NO-7491, Trondheim, Norway
[c] Instituto Nacional de Técnica Aeroespacial (INTA - CEHIPAR), Madrid, Spain
[d] CEHINAV, DITTU, ETSICCyP, Universidad Politécnica de Madrid (UPM), 28040 Madrid, Spain

ARTICLE INFO

Keywords:
Heave forced oscillation tests
Decay tests
Hydrodynamic damping
Added mass
Floating wind turbine
FWT
Renewable energy
Heave plates
Perforated heave plates
Fractal plates

ABSTRACT

The hydrodynamic coefficients (added mass and damping) of oscillating solid and perforated heave plates were investigated using model-scale experiments. Discs with regularly distributed circular holes of various diameters, but with the same overall perforation ratio, were used. Additionally, a fractal geometry incorporating holes of all these diameters was examined. The experiments were conducted in a towing tank using heave force oscillation tests and decay tests using a single degree of freedom mechanism. Potential flow computations performed with WAMIT are also presented. The experimental results are compared to numerical data available in the literature, which suggested that the fractal plate lead to slightly larger damping –a trend not observed in the present study–.

1. Introduction

The use of the seas as a renewable energy source has grown in recent years. In particular, the installation of Floating Wind Turbines (FWTs) is expected to contribute significantly to the ecological transition. FWTs can be installed in deep waters, at depths greater than 50 m. The dynamics of FWT platforms are influenced not only by wind, waves, and ocean currents but also by how these forces interact with and are amplified by the floating platform itself. For instance, the heave natural period of semi-submersible FWT support structures ranges from 17 to 40 s, and at the lower end of this range, it may be affected by first-order wave forces, leading to the possibility of heave resonance. Therefore, the heave motion of offshore platforms has become a wide field of study, as large heave motions can result in fatigue damage to risers, drilling pipes, mooring systems, and increased downtime. At such resonant conditions, damping becomes a critical factor in limiting the response amplitude of these often lightly damped structures.

Solid and perforated heave plates have been widely employed in the offshore industry to improve the dynamic response of platforms, as they can effectively increase the added mass and damping in heave, shifting the natural heave period away from first-order wave energy. Various plate designs, geometries, and configurations have been investigated over the years. Previous research on perforated discs includes both theoretical studies and model tests. Molin (2001) were, to the best of knowledge of the authors, the first to demonstrate that the added mass of perforated plates depends largely on the Keulegan–Carpenter number (KC) and not only the damping. Later, Tao and Dray (2008) conducted forced oscillation tests to investigate the hydrodynamic characteristics of oscillating solid and perforated discs, finding that the added mass significantly decreases as the perforation ratio increases. They also found that solid discs produced the highest damping at large motion amplitudes, corresponding to large KC values. However, at low KC values, perforated plates exhibited the greatest damping. In the experimental and numerical study by An and Faltinsen (2013) of hydrodynamic coefficients for heave plates, similar findings were reported, with good concordance between numerical predictions and experimental results. Tian et al. (2017) provided further benchmarking by examining several geometrical factors of isolated plates, such as thickness ratio, plate shape, edge corners, perforation ratio, and perforated hole size. They

* Corresponding author.
E-mail address: trygve.kristiansen@ntnu.no (T. Kristiansen).

https://doi.org/10.1016/j.apor.2025.104787
Received 2 June 2025; Received in revised form 13 September 2025; Accepted 23 September 2025
Available online 1 October 2025

Fig. 1. Set up of the forced oscillation tests in ETSIN, UPM. The model is attached to the single DoF device.

found no significant influence on the hole sizes tested. More recently, Han et al. (2024) carried out an extensive experimental campaign on vertical circular cylinders with solid and perforated heave plates, analysing surge, heave, and pitch oscillations. Their study highlighted the dominant role of the first harmonic in the hydrodynamic loads, while also showing that higher harmonics become increasingly relevant for large amplitudes and shallow submergence, thus reinforcing the importance of harmonic analysis in these configurations.

Few studies have focused on optimizing the damping performance of heave plates. Wang et al. (2020) carried out numerical simulations of forced oscillations for various heave plates of square shape. They analysed and compared the added mass and damping coefficients for solid plates and regular perforated plates with different shapes and arrangements of holes but with the same perforation ratio of 20%. Additionally, they incorporated fractal perforated plates with perforation ratios from 5% to 20%. Their results indicated that fractal distribution perforated plates exhibited larger damping coefficients than regular distribution with the same perforation ratio, while their added mass remained similar. However, this study lacked experimental validation.

Inspired by the above research, three regular perforated discs with the same perforation ratio but different hole sizes, along with a fractal perforated plate with the same perforation ratio that combines the various hole sizes and replicates the fractal design of Wang et al. (2020), were tested by dedicated experiments in the present study. Forced oscillation tests were conducted at different amplitudes and oscillation frequencies to study the hydrodynamic coefficients of the perforated heave plates. In addition, decay tests were carried out and compared with the results from the forced oscillation tests.

This paper is organized as follows: first, the case study and test matrix are detailed; second, the hydrodynamic model used to extract added mass and damping is presented; third, the results and discussion are provided; and finally, conclusions and future research directions are outlined.

2. Heave forced experiments

2.1. Experimental setup

All experiments were conducted in the ETSIN towing tank at UPM, using a single degree-of-freedom (DoF) system designed to generate vertical motion while minimizing friction and preventing coupled rotations or translations, as described in Medina-Manuel et al. (2022). This system allowed for both harmonic (regular) and arbitrary input signals (irregular) to drive forced oscillation and decay tests. The basin (towing tank) has a length of 100 m and a width of 3.8 m. The water depth in the current experiments was 2.15 m. The model was positioned in the centre of the tank to reduce reflected waves from the tank walls.

Table 1
Main model dimensions.

Characteristic	Symbol	Prototype	Model
Model draft	h	15.5 m	0.775 m
Column diameter	D_c	7.1 m	0.355 m
Heave plate diameter	D_d	20 m	1.0 m
Heave plate thickness	t_d	0.1 m	5 mm
Disc aspect ratio	t_d/D_d	0.005	0.005
Disc depth–radius ratio	h/r_d	1.55	1.55
Column mass	M	663 t	82.83 kg
Disc distance to the tank bottom	h_b	27.5 m	1.375 m
Disc distance to the bottom-disc radius ratio	h_b/r_d	2.75	2.75

Regarding eventual bottom effects, the ratio between the distance to the bottom and the disc radius, h_b/r_d, was 2.75. Therefore, according to the numerical analysis in Garrido-Mendoza et al. (2015), this ratio indicates that bottom effects on the heave plate flow are negligible. In addition, it is expected that viscous damping will be dominant with respect to radiation damping due to the disc depth–radius ratio ($h/r_d = 1.55$) (Lopez-Pavon and Souto-Iglesias, 2015). Fig. 1 illustrates the entire set up in our forced oscillation tests with the model attached to the single DoF system.

Additionally, synchronization tests between the position measurements – obtained using a laser sensor – and load measurements – recorded via a force transducer – revealed a negligible phase delay of approximately 1 ms between the two systems. This confirms that the data acquisition process is accurately synchronized (Kristiansen et al., 2014).

2.2. Case study

The heave plates under study belong to a semi-submersible floating wind turbine design whose second-order surge motions and the scale effects when subjected to heave motions were previously analysed in Simos et al. (2018), Bezunartea-Barrio et al. (2019), respectively. The floater structure consists of three vertical columns linked by trusses. In the present study, only one column scaled model (1:20 scale), equipped with different disc heave plates, was tested. Testing a single individual column is justified by the fact that the distance between the heave plates is significantly larger than the maximum considered full-scale motion amplitude (2.4 m). Since the characteristic length of the vortex shedding is of the order of the motion amplitude (Saettone et al., 2022), the hydrodynamic interaction between the columns during heave motion is not expected to be significant, at least as a first approximation.

The model's main dimensions, including the disc's, are listed in Table 1, both in full and model scale. Further details regarding the considered semisubmersible platform can be found in Simos et al. (2018) and Lopez-Pavon and Souto-Iglesias (2015).

Concerning the discs, one solid (non-perforated) and four interchangeable perforated circular heave plates were built. All perforated plates were designed with the same perforation ratio, $\tau = 20\%$, but different hole size and distribution. The perforation ratio was selected based on the findings of Wang et al. (2020), who used quadrangular plates in their numerical simulations (see Fig. 2). In contrast, circular plates are used in this study to investigate whether geometric differences impact the hydrodynamic performance. The geometries for the perforated plates are provided in Fig. 3, and will be further discussed in Section 2.3. The final disc thickness is 5 mm with a rectangular edge

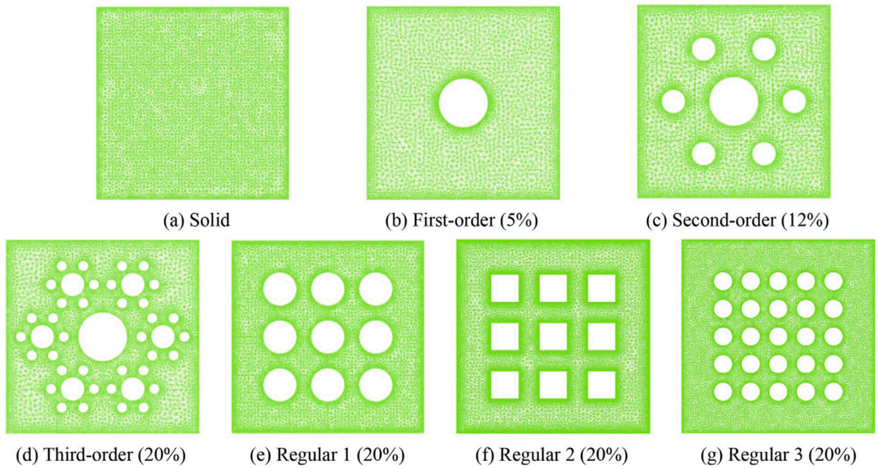

Fig. 2. Grid generations of the heave plates studied by Wang et al. (2020).
Source: Wang et al. (2020).

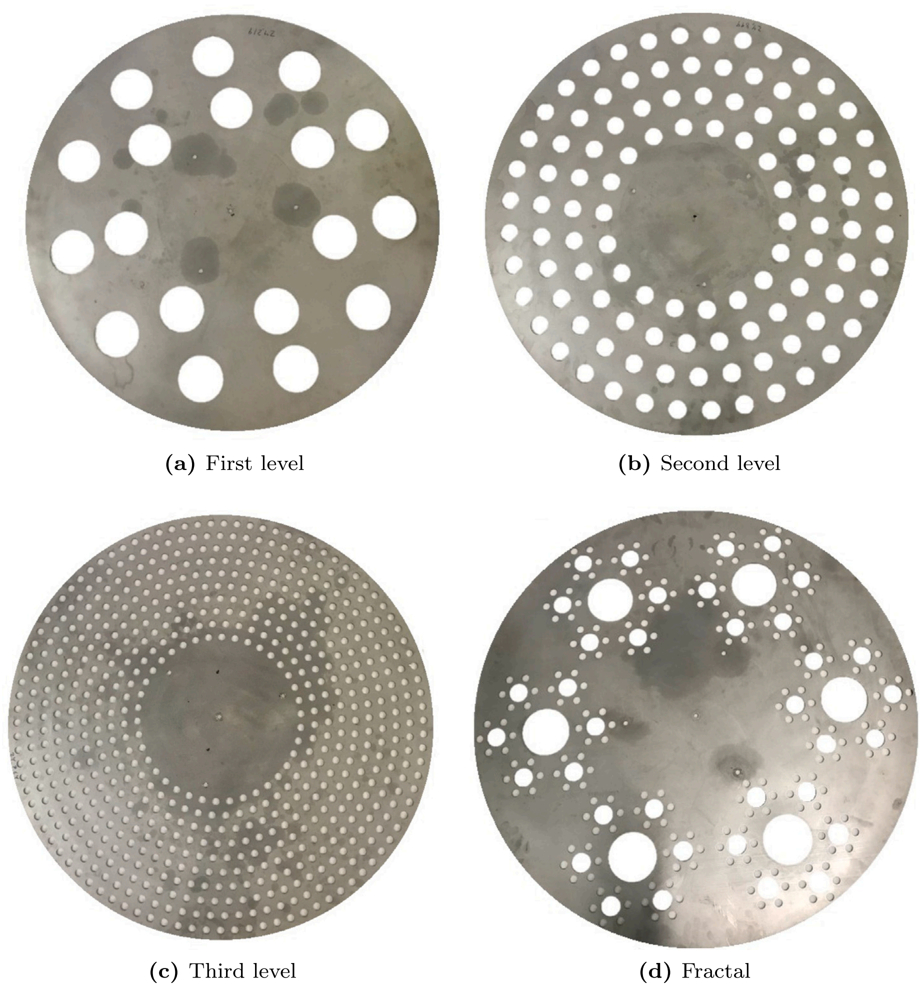

Fig. 3. Perforated plates: specimens.

shape, which may influence the hydrodynamic performance at low KC, as demonstrated by Li et al. (2013).

Before conducting the forced oscillation experiments, a pluck test was performed to determine the natural frequencies of the solid plate. This test revealed natural periods from 5 Hz to 11 Hz, which are outside the range of the oscillation frequencies used in the experiments (0.9 s–3 s), ensuring that the rig's dynamics do not interfere with the test results.

Table 2
Additional test matrix. Sub index m stands for model scale and p for prototype scale.

T_p [s]	A_p [m]	T_m [s]	A_m [mm]	$\beta_m \times 10^5$	KC	$\mathrm{Re}_m \times 10^4$
8.0	0.190	1.79	9.5	5.56	0.06	3.34
8.0	0.318	1.79	15.9	5.56	0.10	5.56
8.0	0.478	1.79	23.9	5.56	0.15	8.35
8.0	0.636	1.79	31.8	5.56	0.20	11.13
8.0	0.796	1.79	39.8	5.56	0.25	13.91

Table 3
Test matrix. Sub index m stands for model scale and p for prototype scale.

T_p [s]	A_p [m]	T_m [s]	A_m [mm]	$\beta_m \times 10^5$	KC	$\mathrm{Re}_m \times 10^5$
4.47	0.32	1.00	15.90	9.96	0.10	1.00
4.47	0.38	1.00	19.10	9.96	0.12	1.20
4.47	0.44	1.00	22.20	9.96	0.14	1.39
4.47	0.51	1.00	25.50	9.96	0.16	1.59
4.47	0.57	1.00	28.60	9.96	0.18	1.79
4.47	0.64	1.00	31.80	9.96	0.20	1.99
4.47	0.76	1.00	38.20	9.96	0.24	2.39
5.59	0.32	1.25	15.90	7.97	0.10	0.80
5.59	0.38	1.25	19.10	7.97	0.12	0.96
5.59	0.44	1.25	22.20	7.97	0.14	1.12
5.59	0.51	1.25	25.50	7.97	0.16	1.27
5.59	0.57	1.25	28.60	7.97	0.18	1.43
5.59	0.64	1.25	31.80	7.97	0.20	1.59
5.59	0.76	1.25	38.20	7.97	0.24	1.91
5.59	0.89	1.25	44.60	7.97	0.28	2.23
5.59	1.02	1.25	50.90	7.97	0.32	2.55
6.71	0.32	1.50	15.90	6.64	0.10	0.66
6.71	0.38	1.50	19.10	6.64	0.12	0.80
6.71	0.44	1.50	22.20	6.64	0.14	0.93
6.71	0.51	1.50	25.50	6.64	0.16	1.06
6.71	0.57	1.50	28.60	6.64	0.18	1.20
6.71	0.64	1.50	31.80	6.64	0.20	1.33
6.71	0.76	1.50	38.20	6.64	0.24	1.59
6.71	0.89	1.50	44.60	6.64	0.28	1.86
6.71	1.02	1.50	50.90	6.64	0.32	2.12
6.71	1.15	1.50	57.30	6.64	0.36	2.39
6.71	1.27	1.50	63.60	6.64	0.40	2.66
6.71	1.40	1.50	70.00	6.64	0.44	2.92
7.83	0.32	1.75	15.90	5.69	0.10	0.57
7.83	0.38	1.75	19.10	5.69	0.12	0.68
7.83	0.44	1.75	22.20	5.69	0.14	0.80
7.83	0.51	1.75	25.50	5.69	0.16	0.91
7.83	0.57	1.75	28.60	5.69	0.18	1.02
7.83	0.64	1.75	31.80	5.69	0.20	1.14
7.83	0.76	1.75	38.20	5.69	0.24	1.37
7.83	0.89	1.75	44.60	5.69	0.28	1.59
7.83	1.02	1.75	50.90	5.69	0.32	1.82
7.83	1.15	1.75	57.30	5.69	0.36	2.05
7.83	1.27	1.75	63.60	5.69	0.40	2.28
7.83	1.40	1.75	70.00	5.69	0.44	2.50
7.83	1.53	1.75	76.4	5.69	0.48	2.73
7.83	1.72	1.75	85.9	5.69	0.54	3.07
8.94	0.32	2.00	15.9	4.98	0.10	0.50
8.94	0.38	2.00	19.1	4.98	0.12	0.60
8.94	0.44	2.00	22.2	4.98	0.14	0.70
8.94	0.51	2.00	25.5	4.98	0.16	0.80
8.94	0.57	2.00	28.6	4.98	0.18	0.90
8.94	0.64	2.00	31.8	4.98	0.20	1.00
8.94	0.76	2.00	38.2	4.98	0.24	1.20
8.94	0.89	2.00	44.6	4.98	0.28	1.39
8.94	1.02	2.00	50.9	4.98	0.32	1.59
8.94	1.15	2.00	57.3	4.98	0.36	1.79
8.94	1.27	2.00	63.6	4.98	0.40	1.99
8.94	1.40	2.00	70.0	4.98	0.44	2.19
8.94	1.53	2.00	76.4	4.98	0.48	2.39
8.94	1.72	2.00	85.9	4.98	0.54	2.69
8.94	1.91	2.00	95.5	4.98	0.60	2.99
8.94	2.23	2.00	111.4	4.98	0.70	3.49
13.94	0.32	3.00	15.9	3.32	0.10	0.33
13.94	0.38	3.00	19.1	3.32	0.12	0.40
13.94	0.44	3.00	22.2	3.32	0.14	0.46
13.94	0.51	3.00	25.5	3.32	0.16	0.53
13.94	0.57	3.00	28.6	3.32	0.18	0.60
13.94	0.64	3.00	31.8	3.32	0.20	0.66
13.94	0.76	3.00	38.2	3.32	0.24	0.80
13.94	0.89	3.00	44.6	3.32	0.28	0.93
13.94	1.02	3.00	50.9	3.32	0.32	1.06
13.94	1.15	3.00	57.3	3.32	0.36	1.20
13.94	1.27	3.00	63.6	3.32	0.40	1.33
13.94	1.40	3.00	70.0	3.32	0.44	1.46
13.94	1.53	3.00	76.4	3.32	0.48	1.59
13.94	1.72	3.00	85.9	3.32	0.54	1.79
13.94	1.91	3.00	95.5	3.32	0.60	1.99
13.94	2.23	3.00	111.4	3.32	0.70	2.32
13.42	2.55	3.00	127.3	3.32	0.80	2.66
13.42	2.86	3.00	143.1	3.32	0.90	2.99

(continued on next page)

Table 3 (continued).

2.3. Regular and fractal perforated plates

As mentioned, four interchangeable perforated circular heave plates were built with the same perforation ratio, $\tau = 20\%$ (see Fig. 3). However, these plates exhibited distinct distributions of the circular perforations (holes). To achieve this diversity, we introduced a scale factor of 0.4 to the diameters of the holes at each plate level, resulting in model-scale perforation diameters of $D_1 = 106.5$ mm, $D_2 = 43$ mm, and $D_3 = 17.5$ mm. The CAD files of each plate tested are given as supplementary material.

The fractal concept was first proposed in the 1970's by the mathematician Benoit Mandelbrot (Mandelbrot, 1983) to describe basic structures with non-integer dimensions and self-similarity. Due to its features in reflecting the objective law of many non linear phenomena and nature shapes, a great deal of research has been carried out in this field, leading to the development of a comprehensive fractal geometry theory (Bhavani and Thanushkodi, 2013; Kim et al., 2013; Cao et al., 2014).

As a consequence, scientists have developed numerous techniques for generating fractal structures, and perforations fractal patterns have been modelled extensively since then. Common fractal models are Sierpinski Gasket or Von Koch Snowflake approach (Mandelbrot, 1983; Khanna and Sharma, 2016). Porous fractal shapes can be created by reproducing a simple pattern with recursive nesting level. This has sparked interest in the application of this theory in many disciplines such as biology, medicine, grid turbulence (Hurst and Vassilicos, 2007; Laizet and Vassilicos, 2011; Omilion et al., 2018), geophysical engineering and telecommunications (Mohan and Sundararajan, 2020). However, there is still a lack of effective research's results of the practical application of the fractal theory in the naval field, and in particular in regards to damping devices for FWTs.

With this aim and inspired by Wang et al. (2020) research, a three nesting level fractal's shape was thus designed. The structure consists of iterative circles with diameters D_1, D_2, and D_3 (see Fig. 3) described before. Moreover, the ratio between holes diameters' centres is 0.33.

2.4. Test matrix

In the present study, the column equipped with circular heave plates was subjected to forced vertical oscillations at specific KC numbers and frequencies, as well as heave free decay tests.

The first aim of the article is to analyse the hydrodynamic coefficients between the solid plates and the different perforated heave plates. For this reason, a test matrix with several KC and β values was proposed (see Table 3).

For each frequency, the maximum feasible amplitude depends on the actuator power, leading to smaller motion amplitudes for higher oscillation frequencies. Considering the dimensions of the tank and the specification of the actuator system, the model tests were carried out in

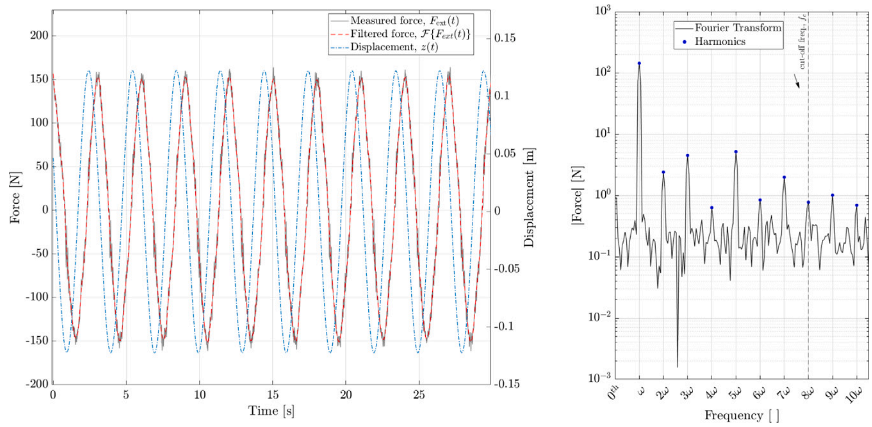

Fig. 4. Force and motions outputs measured in one sample experiment with the fractal plate: $T = 3$ s, KC = 0.754.

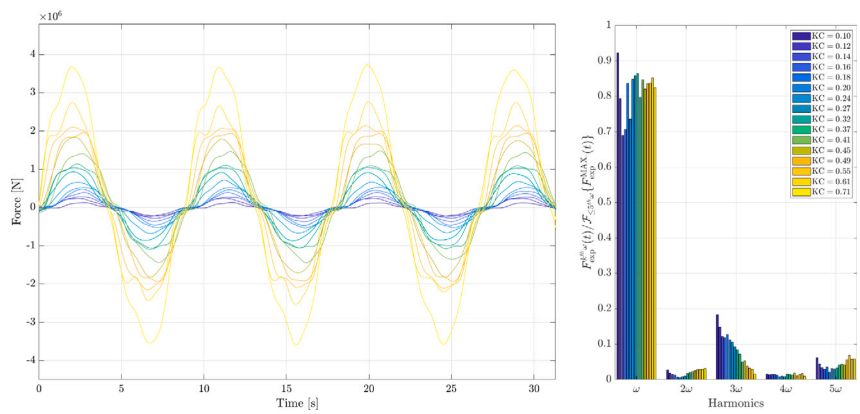

Fig. 5. Filtered force time histories measured for all the KC sample experiments and $T_P = 8.94$ s with third level perforated plate (left). Bar plot of the relative contribution of the first five harmonics, normalized by the maximum experimental force filtered up to the fifth harmonic (right).

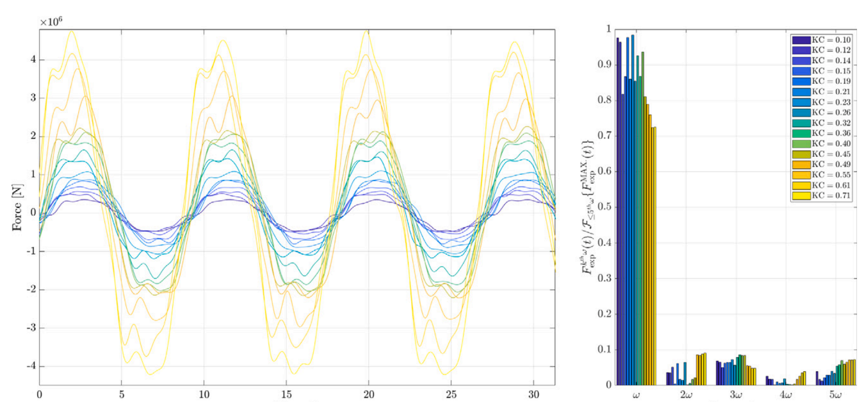

Fig. 6. Filtered force time histories measured for all the KC sample experiments and $T_P = 8.94$ s with solid plate (left). Bar plot of the relative contribution of the first five harmonics, normalized by the maximum experimental force filtered up to the fifth harmonic (right).

the range of KC between 0.1 and 0.8. This range is equivalent to 0.32 m to 2.9 m in terms of full scale displacement amplitudes, representative for the vertical oscillation of the full scale floater in operational and high seas. Another parameter that can be applied to describe the flow condition is β_m, studied in the present work ranging from approximately $3.3 \cdot 10^5$ to $1 \cdot 10^6$ (see Section 3.1).

All tests were performed automatically in a continuous sequence, with sufficient pause time between each test. This automated setup ensured consistent conditions across the tests and minimized potential human error, while the pauses allowed the system to stabilize, reducing any residual effects from previous tests and ensuring reliable data collection.

The second objective of the present work is to compare the numerical simulations done on fractal heave plates by Wang et al. (2020) with experimental results. Hence, the same KC numbers and full scaled period used in Wang et al. (2020) (KC = 0.06, 0.1, 0.15, 0.2 and 0.25 and constant-β = 556434) were included in the test matrix (see Table 2). However, due to geometric differences between Wang's plates and those investigated in the present study, a direct quantitative comparison is not feasible. Specifically, Wang's heave plates feature a quadrangular shape, whereas the plates tested here are circular and include an attached central spar. These geometric variations influence flow patterns, added mass, and damping characteristics, limiting comparisons to qualitative assessments of relative trends and overall performance characteristics.

To evaluate experimental uncertainty, five repetitions were performed at selected amplitudes and frequencies. In addition to the forced oscillation tests, heave decay experiments were conducted with all discs at the same initial KC values.

2.5. Data analysis method

In this work, two types of experiments were considered: forced oscillation tests and free decay tests. Fig. 4 shows a representative force time history, $F_{ext}(t)$, together with the imposed vertical motion readings from the present forced oscillation experiments. . A low-pass filter with a cut-off frequency of 4.5 Hz is applied to the signal to remove spurious contributions from the resonance associated with the natural frequency of the plate.

On the right hand side of Fig. 4, a Fourier analysis of the harmonic content is also presented. The Fourier analysis clearly demonstrates that higher harmonics contribute to the overall load. In the present example, the first harmonic dominates the force response, but higher-order harmonics are visible up to the 10th harmonic. A detailed study of the harmonic content for two chosen plates across the full range of KCs, considering a single representative full scale period of $T_P = 8.94$ s, is shown in Figs. 5 and 6.

Fig. 5 presents the analysed time series from all the force oscillation experiments – single oscillation frequency – and the relative contribution of the first five harmonics for the third level perforated plate. The time histories (left panel) illustrate that the measured force amplitudes increase with increasing motion amplitude, as expected. Although the responses remain close to sinusoidal, deviations from a pure harmonic signal are visible, reflecting the presence of higher-order contributions and experimental noise. The corresponding harmonic decomposition (right panel) quantifies these deviations. The results are displayed as the ratio of the amplitude of each harmonic component, $F_{\text{exp}}^{k^{th}\omega}(t)$, to the maximum experimental force filtered up to the fifth harmonic $\mathcal{F}_{\leq 5^{th}\omega}\{F_{\text{exp}}^{\text{MAX.}}(t)\}$:

$$\frac{F_{\text{exp}}^{k^{th}\omega}(t)}{\mathcal{F}_{\leq 5^{th}\omega}\{F_{\text{exp}}^{\text{MAX.}}(t)\}} \tag{1}$$

The bar plot in Fig. 5 shows that the response is almost entirely concentrated at the fundamental oscillation harmonic, ω, which accounts for more than 85% of the maximum amplitude measured force. Higher order harmonics are negligible in comparison. Among the higher harmonics, the third – and fifth – contribute more strongly than the second and fourth, which is consistent with viscous loads due to sinusoidal oscillations that generate primarily odd harmonics. An example of that is the nonlinear part from drag force in Morison's model, $F_d \propto \dot{z}|\dot{z}|$ (see Eq. (6)). In Appendix A shows that higher odd harmonics can appear with an alternating pattern. However, these harmonics do not influence the response at the fundamental excitation frequency, ω.

As shown in Fig. 5, no systematic trend on the dependence of the first harmonic amplitude on the KC is observed, although a slight increase with KC is observed.

Fig. 6 presents the corresponding results for the solid plate. The overall conclusions remain similar; however, in this case, the first harmonic contribution decreases with increasing KC. Comparable findings were previously reported in Han et al. (2024).

Despite the presence of higher-order harmonics, only the fundamental excitation frequency is used for the analysis of the forced oscillation tests. The reason is that, considering the equation of motion of a floating structure, heave damping plates are primarily included to increase damping at the heave resonance frequency. The effect of higher harmonics is in this respect negligible. Higher harmonic load components can be important for flexible structures in that they may excite natural flexible motions, such as (third-order) ringing loads on a vertical flexible monopile. This experimentally measured force can be modelled as:

$$F_{ext}(t) = \left(M + A_{33}\right)\ddot{z} + B_{33}\dot{z} + C_{33}z, \tag{2}$$

where $z(t)$ is the vertical position described as a sinusoidal function $z(t) = z_0\cos(\omega t)$ with a certain amplitude z_0. M is the model mass, A_{33} is the added mass, B_{33} is the equivalent linear damping, and C_{33} is the static restoring coefficient in heave motion. The hydrodynamic force from Eq. (2) can thus be estimated as:

$$F_H(t) = -A_{33}\ddot{z} - B_{33}\dot{z} = -F_{ext} + M\ddot{z} + C_{33}z. \tag{3}$$

Since the disc is subject to a sinusoidal oscillation, the heave added mass A_{33} and damping coefficient B_{33} for each test are obtained directly from Eq. (3) by Fourier analysis (Garrido-Mendoza et al., 2015; Lopez-Pavon and Souto-Iglesias, 2015). If Eq. (3) is multiplied by $\dot{z}(t)$ and integrated over one, or a whole number of periods, B_{33} is the only term left in the projection:

$$B_{33} = -\frac{\int_t^{t+T} F_H(t)\,\dot{z}(t)\,\mathrm{d}t}{\int_t^{t+T} (\dot{z}(t))^2\,\mathrm{d}t}. \tag{4}$$

The same process is done for A_{33}, but multiplying by $\ddot{z}(t)$:

$$A_{33} = -\frac{\int_t^{t+T} F_H(t)\,\ddot{z}(t)\,\mathrm{d}t}{\int_t^{t+T} (\ddot{z}(t))^2\,\mathrm{d}t}. \tag{5}$$

The equivalent linear damping coefficient B_{33} can also be obtained from the Morison quadratic drag force F_d formula Morison et al. (1950):

$$F_d(t) = -\frac{1}{2}\,\rho\,S_d\,C_d\,\dot{z}(t)\,|\dot{z}(t)|, \tag{6}$$

where $S_d = \pi D_d^2/4$ is the heave plate surface and C_d the drag coefficient. Since the disc is subject to a sinusoidal oscillation, applying Fourier projection techniques of a selected steady-state force history as shown by Sarpkaya and Isaacson (1981), the drag coefficient is given as:

$$C_d = \frac{-3}{4\rho S_d z_0^3\omega^2}\int_t^{t+T} F_H(t)\dot{z}(t)\,\mathrm{d}t. \tag{7}$$

By comparing Eq. (4) and (7), the equivalent linear damping can be expressed as (Tao and Dray, 2008; Tao et al., 2007):

$$B_{33} = \frac{1}{3}\mu\,\beta\,D_d\,C_d\,\mathrm{KC}, \tag{8}$$

with μ being the water dynamic viscosity, β the frequency parameter, and KC the Keulegan–Carpenter number. Frequency parameter is defined as:

$$\beta = \frac{D_d^2 f}{\nu} = \frac{\mathrm{Re}}{\mathrm{KC}}, \tag{9}$$

with f being the frequency in Hertz and ν the kinematic viscosity of water.

The Keulegan–Carpenter number is an especially important non-dimensional quantity in the hydrodynamics of oscillating bodies. It is proportional to the amplitude of the oscillating motion z_0 and inversely proportional to the disc's diameter, D_d:

$$\mathrm{KC} = 2\pi\frac{z_0}{D_d}. \tag{10}$$

The equivalent linear damping formulation (Eq. (3)) is preferred in this study to present results since it is the one used in frequency domain analyses, themselves very practical in the first stages of any floating dynamics study. A quadratic model for the damping could be considered if we are interested in time domain modelling. The interested reader can use Eq. (8) to obtain one from the other.

As in Medina-Manuel et al. (2022), where the same setup was used, the external forces due to air resistance and friction in air bushings are considered negligible in the present research.

In addition to the forced oscillation tests, decay tests were also conducted. In this case, the disc is released from an initial displacement and left to oscillate freely. Each half cycle of the heave response can be approximated to the theoretical solution of a damped single DoF system, as is done by Medina-Manuel et al. (2022). Following the mentioned research (Medina-Manuel et al., 2022), the added mass and damping are then estimated by rearranging the equation as follows:

$$A_{33} = \frac{C_{33}}{\omega_3^2} - M, \tag{11}$$

where ω_3 is the estimate of the heave natural frequency, obtained from the average period between successive peaks in the response signal. And the total dimensional damping:

$$B_{33} = 2\eta\sqrt{\left(M + A_{33}\right) C_{33}}, \tag{12}$$

where η is the non-dimensional damping, defined as a fraction of the critical damping B_{33}^{crit}, which is the damping coefficient above which free decays no longer show oscillatory behaviour.

3. Results and discussion

The hydrodynamic coefficients, i.e. heave added mass and linear equivalent damping coefficient (or its Fourier averaged quadratic drag), A_{33} and B_{33} (C_d), were first obtained using the method described in Section 2.5 based on the force measurements from the forced oscillation experiments. For comparison with other research, the hydrodynamic coefficients in heave, have been made non-dimensional using the theoretical ideal fluid added mass for a disc, which corresponds to the limit at zero KC. Following Sarpkaya and Isaacson (1981), the theoretical added mass of a thin disc oscillating perpendicular to its plane in ideal flow in the low KC limit can be approximated by:

$$A_{33,th} = \frac{1}{3}\rho D_d^3. \tag{13}$$

This theoretical added mass can be corrected by accounting for the central spar, as in Tao et al. (2007), resulting a reduction of around 10% (from 333 to 303 kg, at scale 1:20), which we denote as $A_{33,0} = 0.9A_{33,th}$. The difference is considered large enough so as to maintain this corrected value as the reference one. This yields the added mass non-dimensional coefficient:

$$C_a = \frac{A_{33}}{A_{33,0}}, \tag{14}$$

and the damping coefficient:

$$C_b = \frac{B_{33}}{\omega A_{33,0}}. \tag{15}$$

To compare with the numerical simulations in Wang et al. (2020), one has to bear in mind that the theoretical added mass of a rectangular plate in heave is (see Section 2.5):

$$A_{33,th}^{quad} = 2.609\rho\left(\frac{LB}{\pi}\right)^{3/2}, \tag{16}$$

with L and B being the sides of the plate, ($L = B$ for square shapes). Wang et al. (2020), presented their added mass coefficients, C_m, as follows:

$$C_m = \frac{A_{33}}{\rho L^3}. \tag{17}$$

That means, considering Eqs. (14), (16) and (17), that the coefficients presented herein should be multiplied by a factor of $1/2.13$ to compare values to the ones presented in (Wang et al., 2020):

$$C_a^{quad} = \frac{A_{33}}{A_{33,th}^{quad}} \overset{(16)(17)}{=} C_m \frac{\pi^{3/2}}{2.609}. \tag{18}$$

With the theoretical framework established, we now proceed to present the experimental results. First, the influence of KC and β is discussed, followed by a comparison between the solid and perforated plates, highlighting the effects of hole size and arrangement on the hydrodynamic coefficients. Finally, the results are compared with relevant literature.

3.1. KC and β dependence

As widely discussed in the literature (see e.g., Tao and Dray, 2008; An and Faltinsen, 2013; Tian et al., 2017; Wadhwa et al., 2010), the hydrodynamic coefficients in heave are more strongly influenced by the Keulegan–Carpenter number (KC), which represents the oscillatory motion amplitude, than by the oscillation frequency, which is proportional to the β-parameter. Hence, the present analysis emphasizes the dependence on the KC number. However, β has some implicit relevance due to the presence of a free surface, so although small, there is some frequency-dependency in our results. Different forcing frequencies were also studied to verify the extent of this influence and confirm any impact of β on the outcomes.

Figs. 7 and 8 show the dimensionless added mass and damping coefficients for the tests described in Table 3 for both solid and two of the four perforated plates. They are presented in different β-constant curves as a function of KC number. As an example for the regular perforated plates ($\tau = 20\%$), the second level perforated plate was selected (Figs. 7(b) and 8(b)). The hydrodynamic coefficients for the fractal plate ($\tau = 20\%$) are also presented (Figs. 7(c) and 8(c)). Furthermore, error bars are displayed as the standard deviation between repetitions. For forced oscillation tests, they are not noticeable due to the marginal deviation between tests, indicating negligible random errors. The uncertainty assessment described in Medina-Manuel et al. (2022) could not be followed in this study since different non-dimensional hydrodynamic coefficients have been used. Therefore, as is often the case in model testing, the question of bias error remains unresolved; however, we have no indication of significant bias errors in our results.

Fig. 7 illustrates the influence of the oscillating frequency and motion amplitude on the added mass. It is noticeable that the added mass coefficients, C_a, show no dependence on the frequency parameter β_m, while there is a notable dependence on the Keulegan–Carpenter number. The deviations observed for $\beta_m = 6.64 \cdot 10^5$ curve are attributed to the second harmonic mode of the tank's lateral resonance frequency, approximately at 1.5 s, corresponding to this β_m-value (Medina-Manuel et al., 2022). For the solid plate, the relationship of the heave added mass coefficient and KC appears to be approximately linear. However, this dependence becomes non-linear for both perforated plates, due to the more complex vortex interactions through the holes compared to the simpler vorticity field of the solid plate. This behaviour is consistent with previous findings (Mentzoni and Kristiansen, 2019b).

As shown in previous studies (see e.g. Tao and Dray, 2008), the non-dimensional added mass coefficients for the perforated discs are consistently lower than unity across the range of amplitudes and frequencies tested. This means that the measured added mass is always lower than the theoretical added mass of a solid disc (see Eq. (13)). Further analysis on the effect of perforation on added mass is provided in Section 3.2.

Regarding the damping coefficients, Fig. 8 evidences a similar behaviour to that observed in the added mass coefficients, with C_b primarily influenced by KC. Additionally, the damping coefficient exhibits a non-linear relationship with KC across all plates.

As mentioned, decay tests were also carried out, and their results are included in Figs. 7 and 8. For solid plate, the added mass values obtained from decay tests are consistent with those from forced oscillation tests. Moreover, an offset of unity on the ordinate axis suggests that the added mass approaches the theoretical limit at low KC for the solid plate. However, for perforated plates, agreement is limited to low KC values. At higher KC, discrepancy arises because perforated plates

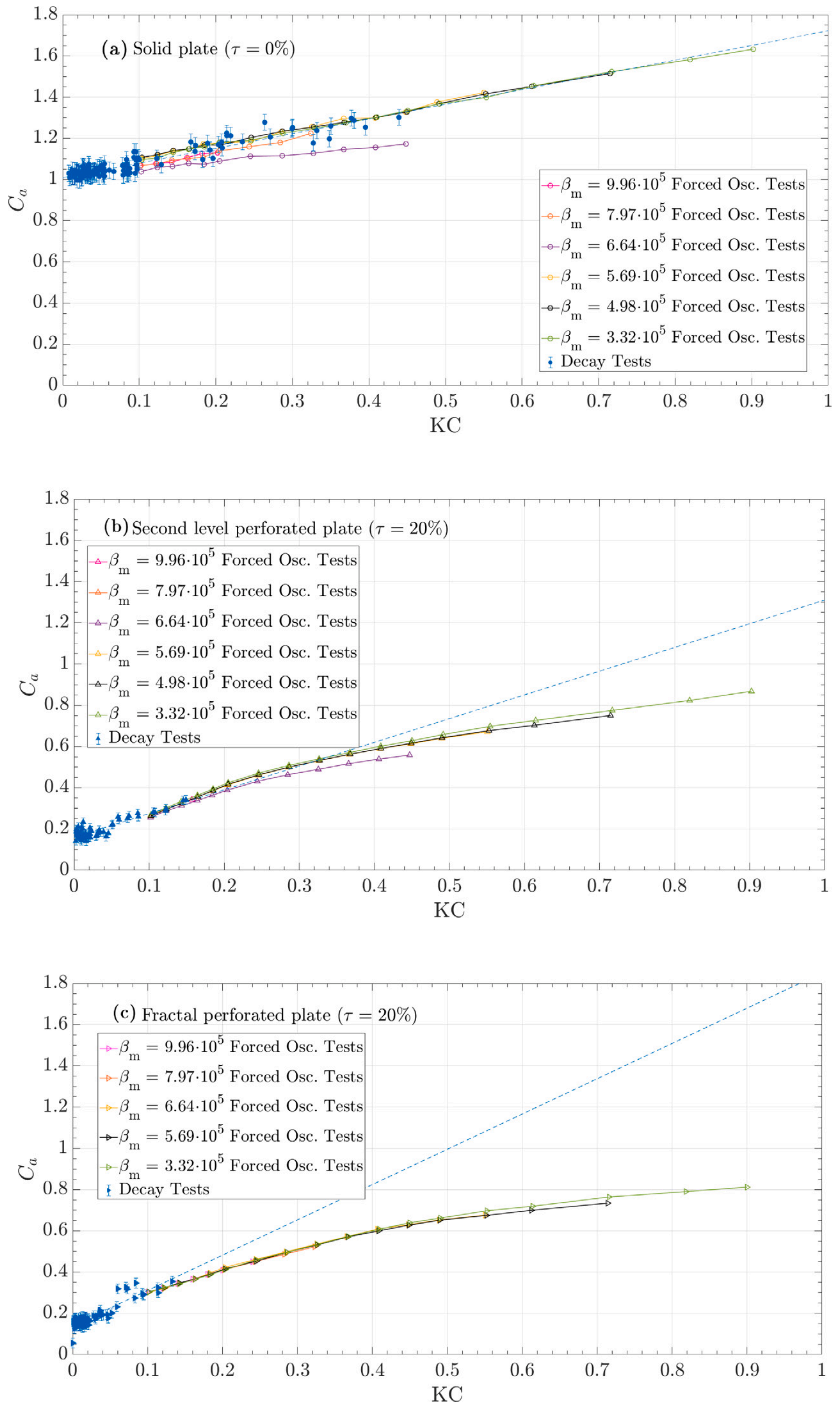

Fig. 7. Experimental results of added mass coefficients for heave plates oscillating at different frequencies. KC and β dependence.

exhibit higher relative damping ratio (η) compared to solid plates, resulting in shorter effective time series (see Fig. 10). Consequently, initial high-amplitude cycles, dominated by transient effects, cannot be fully excluded from the decay test analysis, limiting the reliability of these results for perforated plates. Therefore, forced oscillation tests are recommended over decay tests for characterizing the hydrodynamic behaviour of perforated plates, particularly at higher KC values.

In addition, damping coefficients from the decay tests (Fig. 8) diverge from those obtained through forced oscillation tests due to both reduced reliability and the inherently non-linear behaviour of the damping in perforated plates. Such nonlinearity was previously noted by Tao and Thiagarajan (2003) who identified a slope discontinuity in the damping curve for a solid disc oscillating in still water at KC number around 0.13. In the present study, extrapolating the fitted line (blue dotted line in Fig. 8) of the results obtained from decay tests also reveals a similar discontinuity, which is due to the flow undergoing a transition into a regime of stronger vortex shedding from the plate edges, relative to that for lower KC, where the damping is primarily due to flow separation from the numerous holes (Tao and Thiagarajan, 2003). Similar trends were observed in the present experiments conducted with regular perforated and fractal plates. In these cases, the slope change is more pronounced than in the solid plate, primarily due to the emergence of a blockage effect in the perforated plates, and the role of end-vortex became more significant, especially at larger oscillation amplitudes (see e.g. Molin, 2011; Mentzoni and Kristiansen, 2019a).

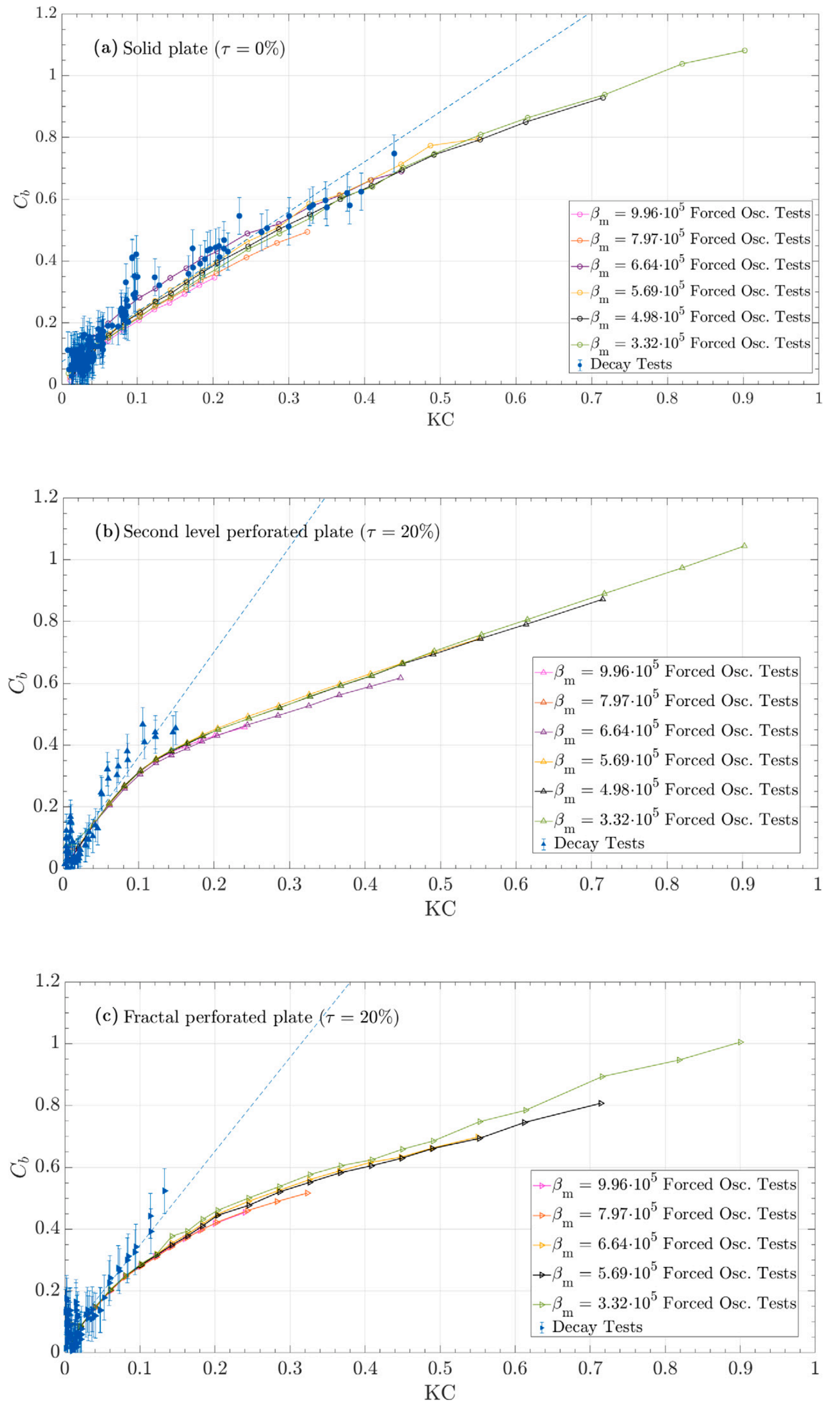

Fig. 8. Experimental results of damping coefficients for heave plates oscillating at different frequencies. KC and β dependence.

3.2. Plate types dependence

In order to analyse the influence of plate type on hydrodynamic coefficients, only a single β curve ($\beta_m = 4.98 \cdot 10^5$ or $T_m = 2$ s) is considered, as the previous section established that frequency dependence is much smaller than amplitude dependence.

The added mass coefficients for both the solid and perforated plates are presented in Fig. 9. Additional data points at low KC values (KC < 0.1) were included to assess the trend of the coefficients in this regime and to enable comparison with the theoretical KC → 0 limit predicted by WAMIT v7.4 potential flow computations (plotted as blue markers) (WAMIT, Inc., 2013). A thorough mesh convergence study was performed for the solid disc, where the meshing procedure is comparatively straightforward. For the perforated plates, however, the meshing process is substantially more elaborate, particularly for smaller opening sizes, and a systematic convergence analysis will be the subject of future work. Nonetheless, the results obtained for the perforated geometries appear consistent with the experimental measurements, lending confidence to the present numerical predictions. The present study does not focus on low-KC behaviour, as a detailed investigation of this range will be addressed in a forthcoming article. Across the full range of KC values, the solid plate exhibits a significantly larger added mass compared to the perforated plates, all of which fall below the theoretical added mass of Eq. (13). This trend is well understood and has been widely reported in the literature, with different perforation ratios (e.g. Tao and Dray, 2008; Tian et al., 2017). In the cases

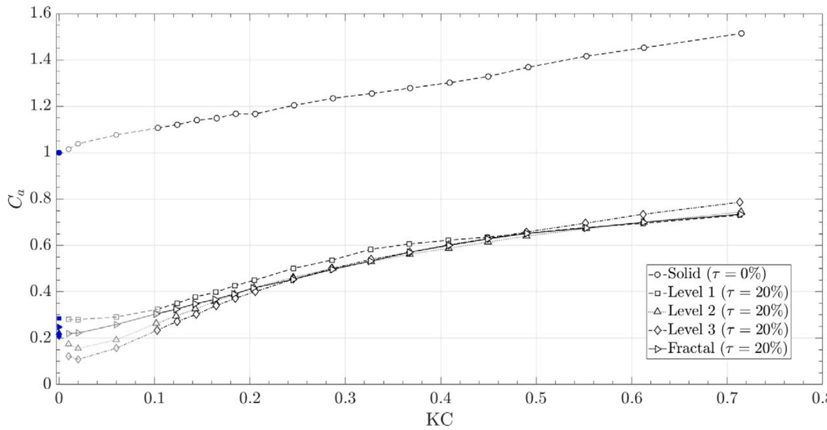

Fig. 9. Experimental results of added mass coefficients for all plates at single $\beta_m = 4.98 \cdot 10^5$. Blue markers at KC = 0 refer to WAMIT results for each plate. Plate type dependence.

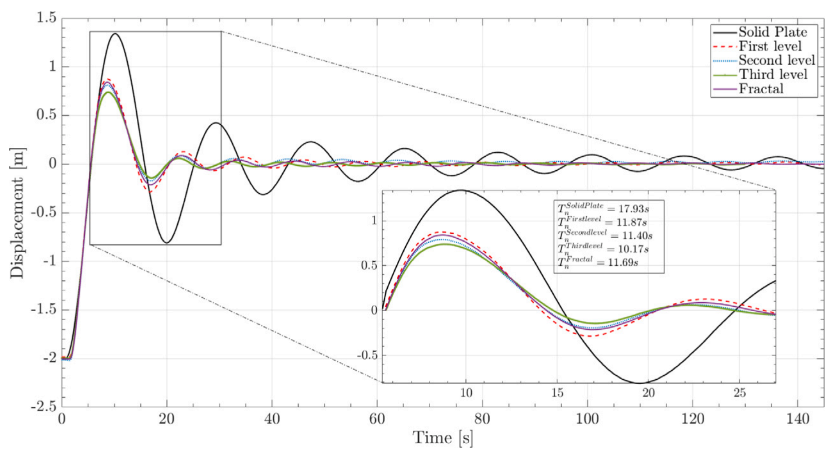

Fig. 10. Time log from decay tests for all the plates tested.

studied herein, the added mass for the perforated plates ($\tau = 20\%$) is approximately 60 – 80% lower than the solid plate. These differences are consistent with those reported by Tao and Dray (2008) and Tian et al. (2017) with solid and perforated plates with the same perforation ratio. Such relative differences become even larger within the low KC number range. As shown in Fig. 9, the experimental data at low KC are consistent with the dimensionless added mass coefficients at infinite frequency, obtained from WAMIT. This consistency supports the reliability of the experimental results.

Regarding the opening size, although all perforated plates, including the fractal design, share the same perforation ratio, their results differ. For KC values above 0.2, the added mass coefficient is effectively independent upon the hole size, except for the third level perforated plate, with minor differences below 7%. Wang et al. (2020) and Tian et al. (2017) also found that the influence of the perforated hole size – or perimeter – on the hydrodynamic coefficients is not significant, being the dominant feature the perforation ratio of the plate. Nevertheless, for KC values below 0.2, such differences become more notable in the present study. At low KC numbers, the first level perforated plate displays the largest added mass and decreases as the opening size decreases, with maximum relative differences of around 20% which is consistent with previous research of Molin (2011).

The time series of one simple decay test with initial KC = 0.6 for each plate is displayed in Fig. 10. For the solid plate, a natural heave period of 17.9 s full-scale was observed, while the first, second, third level, and fractal plates exhibited natural heave periods of 11.9, 11.4, 10.2, and 11.7 s, respectively. These values are consistent with the added mass results found from forced oscillation experiments: the heave natural frequency increases as the perforation ratio increases, something expected as added mass is lower for perforated plates. This outcome indicates that the heave natural frequency of perforated plates may align more closely with first-order operational incident wave frequencies. Furthermore, smaller perforation perimeters will lead to a reduction in added mass and, hence, to a larger heave natural frequency.

Fig. 11 compares non-dimensional damping coefficients of all plates at the same frequency. Several key observations can be made: First, the slope varies among the different plates. Notably, the solid plate yields the steepest slope, while the first level perforated plate displays the one with the least slope. This leads to the second observation: at very low KC numbers, the solid disc produces the lowest C_b compared to the perforated plates. However, at the large KC limit the solid plate's damping exceeds that of all perforated plates except the third level plate. Similar results were also found in Tao and Dray (2008), Tian et al. (2017), where the perforated plates appeared to provide more damping than the solid plate at low KC, i.e. KC $\leq$ 0.6. However, for cases with KC $\geq$ 0.75, the solid plate provided greater damping.

The dependence of C_b on hole shape remains consistent across the range of KC values (KC from 0.1 to 0.9), with damping coefficients for all plates tending to zero as KC approaches zero, as confirmed by WAMIT simulations (blue markers in Fig. 11), meaning there is no wave radiation damping. Plates with larger holes exhibit lower damping, while smaller holes result in higher damping, with maximum relative differences around 30%. This trend arises because increasing the hole size reduces the vortex interactions at the hole edges and the outer plate edge. This observation is aligned with prior studies (Mentzoni

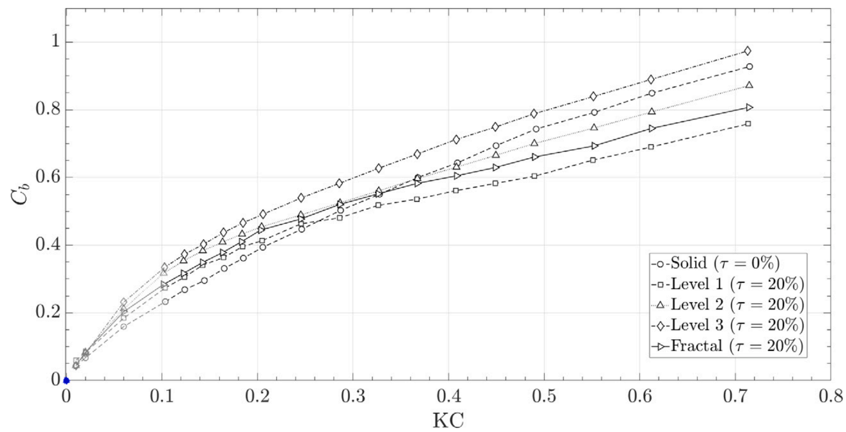

Fig. 11. Experimental results of damping coefficients for all plates at single $\beta_m = 4.98 \cdot 10^5$. Blue markers at KC = 0 refer to WAMIT results for each plate. Plate type dependence.

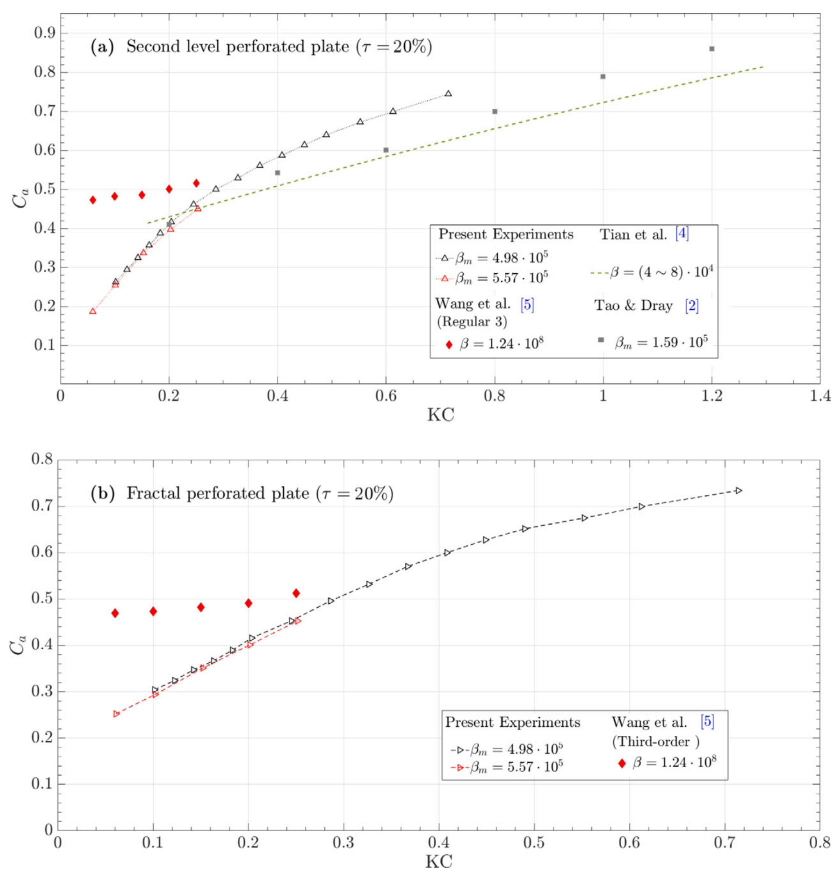

Fig. 12. Experimental results of added mass coefficients compared with reference researches.

and Kristiansen, 2019a; Wang et al., 2020), which also found that a larger perforation perimeter leads to a decrease in damping for a given perforation ratio.

These findings have practical implications, as using heave plates with smaller holes could significantly enhance damping during different conditions. Additionally, the fractal plate is the second last in damping performance, being in between the first and second plates, since it is dominated by the largest holes. However, further investigation is needed to understand the role of hole size distribution and spacing in the damping behaviour of fractal plates.

3.3. Comparison with literature

In this section, our experimental results are compared with those obtained from numerical simulations presented in the Wang et al. (2020) study on fractal plates, which initially motivated the present experimental work. Before presenting the results, one must bear in mind that the cases of study in Wang et al. (2020) were square heave plates, whereas the present study investigated circular plates with a central column. Therefore, the equation used to adjust the coefficients and compare is provided in Eq. (18).

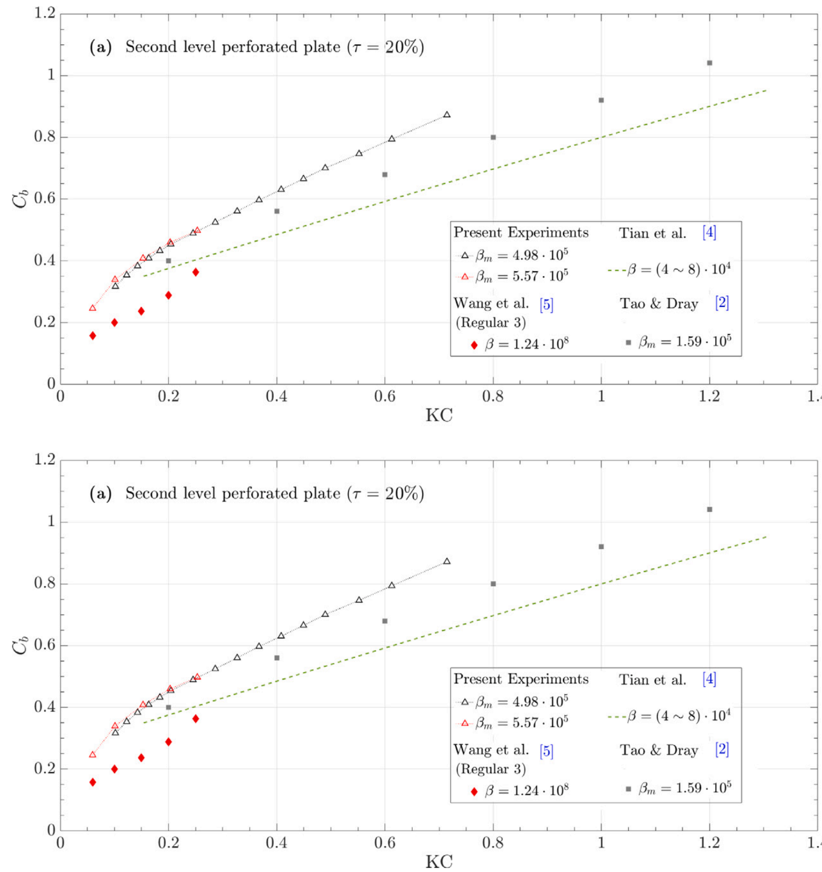

Fig. 13. Experimental results of damping coefficients compared with reference researches.

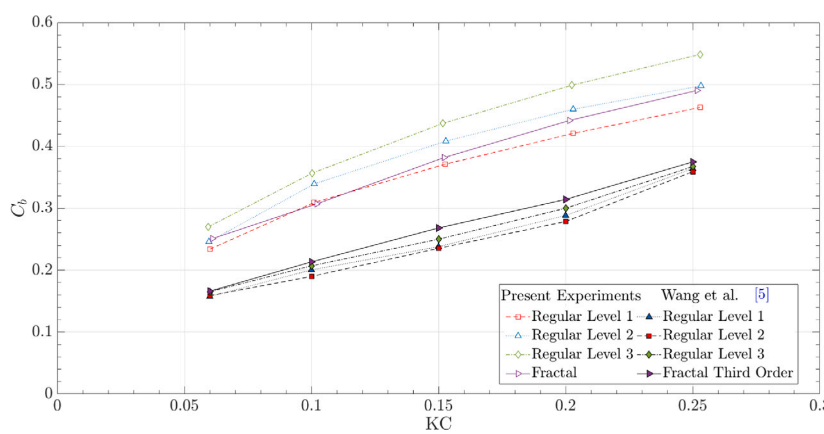

Fig. 14. Comparison of damping coefficients for fractal and regular perforated plates with numerical results from Wang et al. (2020).

Further comparisons are also made with other relevant experimental studies in the literature (Tao and Dray, 2008; Tian et al., 2017); however, these are limited to regular perforated plates featuring the same perforation ratio and similar comparable hole sizes, as the numerical study by Wang et al. (2020) remains the only reference found addressing fractal perforated plates. The hydrodynamic coefficients presented herein differ in their formulation from those used by Tao and Dray (2008) or Tian et al. (2017). While the non-dimensional added mass coefficient coincides with C_a, these authors presented the damping coefficient as:

$$B'_{33_{ref.}} = \frac{B_{33}}{2\omega A_{33,0}}. \tag{19}$$

Thus, to compare with Eq. (15), the values from these works must be multiplied by two to match the same non-dimensionalization.

The dimensionless added mass coefficients for the second level perforated plate and fractal plate are provided in Fig. 12 at T_m = 2 s ($\beta_m = 4.98 \cdot 10^5$). The results presented in Wang et al. (2020) consistently show larger added mass values than the results from this study. However, as the oscillation amplitude increases, the values tend to align more closely. One contribution to the discrepancies may be the disparities in β values, which are of the order of $5 \cdot 10^5$ in present experiments compared to $1 \cdot 10^8$ in Wang et al. (2020) (see Section 3.1). Another contributing factor is the square shape of the heave plate studied in Wang et al. (2020). Similar discrepancies in added mass were noted by Wang et al. (2020) when comparing to other literature references (Liu et al., 2012; Shen et al., 2011) in their Fig. 8.

By contrasting our experimental added mass results of the second level perforated plate (see Fig. 12(a)) with Tao and Dray (2008) and Tian et al. (2017) results, we find a reasonable degree of agreement. Although the frequency parameter differs between studies, and higher KC values were investigated in both Tao and Dray (2008) and Tian et al. (2017), the overall trends remain consistent.

Fig. 13 compares the dimensionless damping coefficients. Both the second level (Fig. 13(a)) and fractal (Fig. 13(b)) show larger damping than those reported in Wang et al. (2020). Once again, different plate shapes may explain part of the differences. According to recent experimental research (Zhang et al., 2023), compared to other shapes, square heave plates exhibit the lowest damping coefficients when the KC number is below 0.9, which may explain the observed differences.

It is worth noting that the damping coefficients from the second-level perforated plate in this study are in fair agreement with other experimental data from the literature (see Fig. 13(a)).

Fig. 14 provides a direct comparison between the damping coefficients for all the perforated plates obtained in the present study (Tables 2) and those from Wang et al. (2020), matching identical full-scale periods and KC numbers.

Wang et al. (2020) observed that the third-order fractal plate displayed the highest damping along all the KCs simulated. In contrast, the present study shows that the fractal perforated plate yields a lower C_b than that of the second and third-level regular perforated plates.

As discussed in Section 3.2 the regular perforated plates display a similar trend to those observed by Wang et al. (2020), where decreasing the perimeter of the perforation region increases damping for the same perforation ratio. However, the present experiments yielded higher damping values across all plates compared to Wang et al. (2020).

4. Conclusions

In this study, a solid disc and four perforated discs with regular hole distributions, along with one featuring a fractal distribution, were subjected to forced heave oscillation and decay tests. From our analysis of the experimental results, complemented with a comparative assessment with existing numerical data available in the literature, the following conclusions were drawn:

1. The solid plate consistently exhibited higher added mass coefficients compared to perforated plates, which typically fell below the theoretical added mass of a solid disc. The relationship of the heave added mass coefficient and KC appeared to be approximately linear for the solid plate, while nonlinear trends were showed for the perforated plates.
2. Damping coefficients exhibited a slope discontinuity at KC number around 0.13 correlation, though the slope varied among the different plates. The solid disc produced the lowest damping at very low KC values compared to the perforated plates. However, as KC numbers increased, the solid plate's damping surpassed that of the perforated plates, except for the third-level perforated plate.
3. While the size of the openings had a relatively minor influence on added mass coefficients, its impact on damping coefficients was appreciable. Perforated plates generally showed increasing damping as hole size decreased. Fractal plates demonstrated behaviour akin to perforated plates, with some differences in the damping coefficient.
4. The experimental outcomes aligned closely with previous experimental studies. However, disparities emerged when comparing them to available simulation results, particularly in added mass coefficients. These tended to be larger, especially at low KC numbers. Additionally, simulation results for damping coefficients of perforated plates consistently predicted lower values than present experimental observations. These disparities were attributed to the shape of the disc, the selection of oscillation frequency among numerical parameters.

Finally, regarding the fractal plate, the results presented herein evinced that the use of fractal holes distribution does not bring significant benefits in terms of added mass or damping. However, detailed numerical studies may be necessary to gain a more comprehensive understanding of the specific advantages or characteristics associated with fractal hole distributions. Future research should extend study in lower KC numbers (≤ 0.1).

CRediT authorship contribution statement

Antonio Medina-Manuel: Writing – review & editing, Writing – original draft, Methodology, Investigation, Formal analysis, Data curation, Conceptualization. **Trygve Kristiansen:** Writing – review & editing, Supervision, Methodology, Investigation, Formal analysis. **Adolfo Maron-Loureiro:** Investigation, Conceptualization. **Rafael Molina Sánchez:** Investigation, Conceptualization. **Antonio Souto-Iglesias:** Writing – review & editing, Supervision, Resources, Project administration, Methodology, Investigation, Funding acquisition, Conceptualization.

Declaration of competing interest

The authors declare that they have no known competing financial interests or personal relationships that could have appeared to influence the work reported in this paper.

Acknowledgements

The authors acknowledge the funding received from the Research Council of Norway through SFI BLUES, grant number 309281. This research has also been partially funded by the Ministry of Science and Innovation of Spain through the projects FOWT-DAMP2 (Reference: PID2021-123437OB-C21) and ESOMOOR (Reference: PCI2024-155038-2). The authors would also like to thank Juan Luis Chacón for his help with various aspects in this initiative and express their gratitude to Mael Moreau for conducting the numerical simulations. For further details on the potential flow simulations conducted using WAMIT v7.4 please contact with mael.k.i.moreau@ntnu.no.

Appendix A. Fourier expansion of the nonlinear drag term in Morison's model

Following Morison et al. (1950), the equation for Morison's drag force is expressed in Eq. (6). Assuming a sinusoidal vertical motion $z(t) = z_0 \cos(\omega t)$, we can expand the right hand side equation:

$$f(t) = \dot{z}\,|\dot{z}| = -\left(z_0\omega\right)^2 \sin(\omega t)\,|\sin(\omega t)|, \tag{20}$$

into its Fourier series Bracewell (1966). Given that the function is odd, $f(-t) = -f(t)$, its Fourier series only contains sine terms. Its coefficients b_n can be computed as twice the integral over $[0, \pi]$:

$$b_n = \frac{2}{\pi}\int_0^{\pi} f(t)\sin(n\omega t)\,\mathrm{d}t, \tag{21}$$

due to half-wave antisymmetry, $f(t+\pi) = -f(t)$. Applying $f(t) = \sin^2(\omega t)$ for $t \in [0, \pi]$ and using the product to sum identity in Eq. (21):

$$\begin{aligned} b_n &= \frac{2}{\pi}\int_0^{\pi} \sin^2(\omega t)\sin(n\omega t)\,\mathrm{d}t \\ &= \frac{2}{\pi}\int_0^{\pi} \frac{1-\cos(2\omega t)}{2}\sin(n\omega t)\,\mathrm{d}t \\ &= \frac{2}{\pi}\int_0^{\pi} \left[\frac{1}{2}\sin(n\omega t) - \frac{1}{2}\sin(n\omega t)\cos(2\omega t)\right]\mathrm{d}t \\ &= \frac{2}{\pi}\left[\frac{1}{2}\int_0^{\pi}\sin(n\omega t)\,\mathrm{d}t - \frac{1}{4}\int_0^{\pi}\left(\sin\left((n+2)\omega t\right) + \sin\left((n-2)\omega t\right)\right)\mathrm{d}t\right]. \end{aligned} \tag{22}$$

For any integer $k \geq 1$,

$$\int_0^{\pi} \sin(kt)\,\mathrm{d}t = \frac{1-(-1)^k}{k}. \tag{23}$$

The general expression for the sine Fourier coefficients leads as follows:

$$b_n = \frac{2}{\pi}\left[\frac{1}{2}\frac{1-(-1)^n}{n} - \frac{1}{4}\left(\frac{1-(-1)^{n+2}}{n+2} + \frac{1-(-1)^{n-2}}{n-2}\right)\right]. \tag{24}$$

This remains only the odd sine harmonics for these coefficients, since if n is odd $1-(-1)^n = 2$ and $1-(-1)^{n+2}$, but if n is even, $1-(-1)^n = 0$ and the whole expression collapses to $b_n = 0$. Thus, the final Fourier expansion for the function $f(t)$ from Eq. (20) may be written in its closed form as:

$$f(t) = -\left(z_0\omega\right)^2 \sum_{n=1}^{\infty}\left(\frac{-8}{\pi\, n\left(n^2-4\right)}\right)\sin(n\omega t). \tag{25}$$

And its explicit form for the first harmonic terms:

$$f(t) = -\left(z_0\omega\right)^2\left[\frac{8}{3\pi}\sin(\omega t) - \frac{8}{15\pi}\sin(3\omega t) - \frac{8}{105\pi}\sin(5\omega t) - \cdots\right]. \tag{26}$$

Consequently, the shape of this expression confirms that the drag term of the Morison load model results in a load containing all odd harmonics, where the first is dominant, being for instance five times as high as the third harmonic. Only the first harmonic contribution is retained in the process of equivalent linearization, something which is a consequence of the orthogonality of cosines.

Regarding even harmonics being present in the measured force time-series, they are a consequence of that the physics is more complex than that modelled by the Morison equation. However, it is interesting to note that the amplitude of the odd harmonic components are in general higher than those of the even harmonic components.

Appendix B. Supplementary data

Supplementary multimedia files are provided with this article. Visit http://mega.nz/folder/qMBHACwB#VFqt0dzwKnzPIWtvECb2sA to watch videos of the system in operation during forced oscillation experiments and decay tests. The CAD geometries of the heave plates can be found in the mentioned link. The data that support the findings of this study are available from the corresponding author upon reasonable request.

References

An, Song, Faltinsen, Odd, 2013. An experimental and numerical study of heave added mass and damping of horizontally submerged and perforated rectangular plates. J. Fluids Struct. 39, 87–101. http://dx.doi.org/10.1016/j.jfluidstructs.2013.03.004.

Bezunartea-Barrio, Ana, Fernandez-Ruano, Sergio, Maron-Loureiro, Adolfo, Molinelli-Fernandez, Enrique, Moreno-Buron, Francisco, Oria-Escudero, Julio, Rios-Tubio, Jose, Soriano-Gomez, Cristina, Valea-Peces, Alvaro, Lopez-Pavon, Carlos, Souto-Iglesias, Antonio, 2019. Scale effects on heave plates for semi-submersible floating offshore wind turbines: Case study with a solid plain plate. J. Offshore Mech. Arct. Eng. (ISSN: 0892-7219) 142 (3), http://dx.doi.org/10.1115/1.4045374, 031105.

Bhavani, Sridharan, Thanushkodi, Kepanna Gowder, 2013. Comparison of fractal coding methods for medical image compression. IET Image Process. 7 (7), 686–693. http://dx.doi.org/10.1049/iet-ipr.2012.0041, arXiv:https://ietresearch.onlinelibrary.wiley.com/doi/pdf/10.1049/iet-ipr.2012.0041.

Bracewell, Ronald N., 1966. The Fourier transform and its applications. In: MCGraw-Hill. URL https://api.semanticscholar.org/CorpusID:18010056.

Cao, Guangxi, Cao, Jie, Xu, Longbing, He, LingYun, 2014. Detrended cross-correlation analysis approach for assessing asymmetric multifractal detrended cross-correlations and their application to the Chinese financial market. Phys. A (ISSN: 0378-4371) 393, 460–469. http://dx.doi.org/10.1016/j.physa.2013.08.074.

Garrido-Mendoza, Carlons, Thiagarajan, Krish, Souto-Iglesias, Antonio, Colagrossi, Andrea, Bouscasse, Benjamin, 2015. Computation of flow features and hydrodynamic coefficients around heave plates oscillating near a seabed. J. Fluids Struct. (ISSN: 0889-9746) 59, 406–431. http://dx.doi.org/10.1016/j.jfluidstructs.2015.10.003.

Han, Seung-Yoon, Bouscasse, Benjamin, Leroy, Vincent, Delacroix, Sylvain, Gilloteaux, Jean-Christophe, Bonnefoy, Félicien, Le Touzé, David, 2024. Experimental study of hydrodynamic loads induced by the motion of a vertical circular cylinder with heave plates in proximity of the free surface. Ocean Eng. (ISSN: 0029-8018) 310, 118712. http://dx.doi.org/10.1016/j.oceaneng.2024.118712.

Hurst, Daryl, Vassilicos, J.C., 2007. Scalings and decay of fractal-generated turbulence. Phys. Fluids 19 (3), 035103. http://dx.doi.org/10.1063/1.26764482.

Khanna, Ghriti, Sharma, Narinder, 2016. Fractal antenna geometries: A review. Int. J. Comput. Appl. 153, 29–32. http://dx.doi.org/10.5120/ijca2016912106.

Kim, Paul Y., Iftekharuddin, Khan M., Davey, Pinakin G., Tóth, Márta, Garas, Anita, Holló, Gabor, Essock, Edward A., 2013. Novel fractal feature-based multiclass glaucoma detection and progression prediction. IEEE J. Biomed. Heal. Informatics 17 (2), 269–276. http://dx.doi.org/10.1109/TITB.2012.2218661.

Kristiansen, Trygve, Ruth, Eivind, Firoozkoohi, Reza, Borgen, Henning, Berge, Bjørn, 2014. Experimental and numerical investigation of ship roll damping with and without bilge keels. In: Proceedings of the International Conference on Offshore Mechanics and Arctic Engineering - OMAE, vol. 1, http://dx.doi.org/10.1115/OMAE2014-24585.

Laizet, Sylvain, Vassilicos, J., 2011. DNS of fractal-generated turbulence. Flow Turbul. Combust. 87, 673–705. http://dx.doi.org/10.1007/s10494-011-9351-2.

Li, Jinxuan, Liu, Shuxue, Zhao, Min, Teng, Bin, 2013. Experimental investigation of the hydrodynamic characteristics of heave plates using forced oscillation. Ocean Eng. (ISSN: 0029-8018) 66, 82–91.

Liu, Shu-Xue, Zhao, Min, Li, Jin-Xuan, Teng, Bin, 2012. Experimental investigations of hydrodynamic characteristics of the perforated heave plates. Shuidonglixue Yanjiu Yu Jinzhan/Chinese J. Hydrodyn. Ser. A 27 (3), 248–255, URL https://www.scopus.com/inward/record.uri?eid=2-s2.0-84863226922&partnerID=40&md5=a4183d029fdd2819381374fce224fc25.

Lopez-Pavon, Carlos, Souto-Iglesias, Antonio, 2015. Hydrodynamic coefficients and pressure loads on heave plates for semi-submersible floating offshore wind turbines: A comparative analysis using large scale models. Renew. Energy (ISSN: 0960-1481) 81, 864–881. http://dx.doi.org/10.1016/j.renene.2015.04.003.

Mandelbrot, Benoit B., 1983. The fractal geometry of nature. Einaudi paperbacks, Henry Holt and Company, ISBN: 9780716711865, URL https://books.google.es/books?id=0R2LkE3N7-oC.

Medina-Manuel, Antonio, Botia-Vera, Elkin, Saettone, Simone, Calderon-Sanchez, Javier, Bulian, Gabriele, Souto-Iglesias, Antonio, 2022. Hydrodynamic coefficients from forced and decay heave motion tests of a scaled model of a column of a floating wind turbine equipped with a heave plate. Ocean Eng. (ISSN: 0029-8018) 252, 110985. http://dx.doi.org/10.1016/j.oceaneng.2022.110985, URL https://www.sciencedirect.com/science/article/pii/S0029801822004115.

Mentzoni, Fredrik, Kristiansen, Trygve, 2019a. Numerical modeling of perforated plates in oscillating flow. Appl. Ocean Res. (ISSN: 0141-1187) 84, 1–11. http://dx.doi.org/10.1016/j.apor.2018.12.016, URL https://www.sciencedirect.com/science/article/pii/S0141118718306527.

Mentzoni, Fredrik, Kristiansen, Trygve, 2019b. A semi-analytical method for calculating the hydrodynamic force on perforated plates in oscillating flow. http://dx.doi.org/10.1115/OMAE2019-95093.

Mohan, Anand, Sundararajan, M., 2020. Fractal antenna – wireless communication new beginning breakthrough in digital era. Acta Inform. Malays. 4, 01–06. http://dx.doi.org/10.26480/aim.01.2020.01.06.

Molin, Bernard, 2001. On the added mass and damping of periodic arrays of fully or partially porous disks. J. Fluids Struct. (ISSN: 0889-9746) 15 (2), 275–290. http://dx.doi.org/10.1006/jfls.2000.0338.

Molin, Bernard, 2011. Hydrodynamic modeling of perforated structures. Appl. Ocean Res. (ISSN: 0141-1187) 33 (1), 1–11. http://dx.doi.org/10.1016/j.apor.2010.11.003.

Morison, J.R., Johnson, J.W., Schaaf, S.A., 1950. The force exerted by surface waves on piles. J. Pet. Technol. (ISSN: 0149-2136) 2 (05), 149–154. http://dx.doi.org/10.2118/950149-G, arXiv:https://onepetro.org/JPT/article-pdf/2/05/149/2238818/spe-950149-g.pdf.

Omilion, Alexis, Turk, Jodi, Zhang, Wei, 2018. Turbulence enhancement by fractal square grids: Effects of multiple fractal scales. Fluids 3, 37. http://dx.doi.org/10.3390/fluids3020037.

Saettone, Simone, Molinelli, Enrique, Fernández, Cristina, Saavedra, Leandro, Duque, Daniel, Souto-Iglesias, Antonio, Maron, Adolfo, 2022. A particle image velocimetry investigation of the flow field close to a heave plate for models of different scales. Appl. Ocean Res. (ISSN: 0141-1187) 129, 103387. http://dx.doi.org/10.1016/j.apor.2022.103387.

Sarpkaya, T., Isaacson, M., 1981. Mechanics of wave forces on offshore structures. van Nostrand Reinhold, New York.

Shen, Wen-Jun, Tang, You-Gang, Zhao, Jing-Rui, 2011. Hydrodynamic characteristics of heave plate structure for truss spar. Tianjin Daxue Xuebao (Ziran Kexue Yu Gongcheng Jishu Ban)/Journal of Tianjin Univ. Sci. Technol. 44 (6), 491–496, URL https://www.scopus.com/inward/record.uri?eid=2-s2.0-80052551408&partnerID=40&md5=c591c4e5bd7ad6305e80610ded90d599.

Simos, Alexandre Nicolaos, Ruggeri, Felipe, Watai, Rafael A., Souto-Iglesias, Antonio, Lopez-Pavon, Carlos, 2018. Slow-drift of a floating wind turbine: An assessment of frequency-domain methods based on model tests. Renew. Energy 116 (Part A), 133–154. http://dx.doi.org/10.1016/j.renene.2017.09.059.

Tao, Longbin, Dray, Daniel, 2008. Hydrodynamic performance of solid and porous heave plates. Ocean Eng. 35 (10), 1006–1014. http://dx.doi.org/10.1016/j.oceaneng.2008.03.003.

Tao, L., Molin, B., Scolan, Y.-M., Thiagarajan, K., 2007. Spacing effects on hydrodynamics of heave plates on offshore structures. J. Fluids Struct. (ISSN: 0889-9746) 23 (8), 1119–1136. http://dx.doi.org/10.1016/j.jfluidstructs.2007.03.004.

Tao, Longbin, Thiagarajan, Krish, 2003. Low KC flow regimes of oscillating sharp edges. II. Hydrodynamic forces. Appl. Ocean Res. (ISSN: 0141-1187) 25 (2), 53–62. http://dx.doi.org/10.1016/S0141-1187(03)00046-4.

Tian, Xinliang, Tao, Longbin, Li, Xin, Yang, Jianmin, 2017. Hydrodynamic coefficients of oscillating flat plates at $0.15 \leq KC \leq 3.15$. J. Mar. Sci. Technol. 22, 101–113. http://dx.doi.org/10.1007/s00773-016-0401-2.

Wadhwa, H., Krishnamoorthy, B., Thiagarajan, K. P., 2010. Variation of heave added mass and damping near seabed. In: ASME 29th International Conference on Offshore Mechanics and Arctic Engineering, OMAE.

WAMIT, Inc., 2013. WAMIT user manual, version 7.4. URL https://www.wamit.com/manualupdate/v74_manual.pdf.

Wang, Bo, Xu, Zifei, Li, Chun, Wang, Donghua, Ding, Qinwei, 2020. Hydrodynamic characteristics of forced oscillation of heave plate with fractal characteristics based on floating wind turbine platform. Ocean Eng. 212, 107621. http://dx.doi.org/10.1016/j.oceaneng.2020.107621.

Zhang, Lixian, Shi, Wei, Zeng, Yuxin, Michailides, Constantine, Zheng, Siming, Li, Ying, 2023. Experimental investigation on the hydrodynamic effects of heave plates used in floating offshore wind turbines. Ocean Eng. (ISSN: 0029-8018) 267, 113103. http://dx.doi.org/10.1016/j.oceaneng.2022.113103.